Composite Structures 384 (2026) 120171

Contents lists available at ScienceDirect

Composite Structures

journal homepage: www.elsevier.com/locate/compstruct

Review

Printing bending pneumatic artificial muscles with variable stiffness and curvature: Theoretical, simulation and experimental results

Zhengyue Li [a], Jian Sun [b], Yanju Liu [a,*], Jinsong Leng [b]

[a] Department of Astronautical Science and Mechanics, Harbin Institute of Technology, Harbin, 150001, China
[b] Center for Composite Materials and Structures, Harbin Institute of Technology, Harbin, 150080, China

ARTICLE INFO

Keywords:
Pneumatic artificial muscle
Shape memory polymer
4D printing

ABSTRACT

Soft actuators, capable of mimicking the motion of biological organisms, enable precise and gentle operations in complex environments. While conventional pneumatic artificial muscles (PAMs) are typically fabricated from materials with fixed stiffness, this study introduces shape-memory polymers (SMPs) to achieve tunable stiffness, thereby enhancing both deformability and load-bearing capacity. By replacing traditional bladders and constraint frameworks with 3D-printed SMP structures, we have developed SMP-PAMs that exhibit temperature-controlled bending and elongation. We analyze the kinematics of the printed PAM, evaluate its output force and bending moment at varying temperatures. A nonlinear quasi-static model, based on the virtual work principle, is developed to capture the interaction between pneumatic input and structural mechanics and its effect on actuation performance. Finite element analysis (FEA) is employed to simulate the PAM's motion, where a full-scale braided tube is first modeled, followed by a simplified equivalent cross-section model for coupled simulation with the internal elastomer. Experimental validation confirms the SMP-PAM's shape recovery rate, temperature response, kinematic deformation, and bending stiffness. Through a combination of theoretical modeling, simulation, and experiments, this study provides a comprehensive performance evaluation of the novel PAM, offering key insights for future research and innovative design approaches.

1. Introduction

Soft actuators play a vital role in the functionality of soft robots, significantly improving the flexibility and safety of robotic systems [1,2]. By imitating the compliant motion of living organisms [3], they allow for stretching [4], bending [5], and twisting [6], which facilitates precise and gentle manipulation in dynamic settings and reduces the risk of damage to nearby objects. This technology not only broadens the scope of robotic applications in healthcare [7–10], service industries [11], and precision manufacturing but also enhances the interaction between humans and robots in daily life and industrial environments, making it a crucial force in the evolution of robotics [12,13].

Braided pneumatic artificial muscles (PAMs) are a quintessential type of soft actuators [14,15], comprising a flexible inner liner, a braided tube, elastic beams, and connecting components [16]. Traditionally, these components are designed with fixed stiffness [17]. However, the ability to adjust the stiffness of each component or the entire assembly in a controlled manner would greatly increase the adaptability of braided PAMs [18,19]. By incorporating variable stiffness, pneumatic artificial muscles can achieve greater deformation capabilities, enhanced load-bearing strength, and a wider range of motion patterns.

Jianbin Liu designed a triple helix balloon weaving and shape memory polymer (SMP) skeleton mechanism that allows for agile actuation and variable stiffness functionality [20]. Kazuto Takashima developed a segmented SMP sheet embedded with electric heating wires and evaluated its mechanical properties through bending and tensile tests [21,22]. By applying SMP sheets embedded with electric heating wires to pneumatic synthetic rubber muscles [23,24], the initial shape and bending displacement of these muscles can be controlled by adjusting the temperature of the SMP sheets [25]. Rossiter J explores the use of SMP resin to impregnate the woven mesh shell of commercial McKibben artificial muscles. When the actuator reaches the required length, SMP can be cooled below its glass transition temperature (T_g), and it will fix the structure in a rigid state. J. describes how twisted polymer artificial muscles are integrated into Fan precursor fibers to serve as driving mechanisms [21]. Shigeyoshi Yahara proposed a shape memory polymer (SMP) technique alongside layer interference (LJ) method to achieve simultaneous response of soft robots. This is

* Corresponding author.
E-mail address: yj_liu@hit.edu.cn (Y. Liu).

https://doi.org/10.1016/j.compstruct.2026.120171
Received 29 October 2025; Received in revised form 28 January 2026; Accepted 19 February 2026
Available online 20 February 2026

Table 1
Comparison of Feature between SMP-PAM and Conventional PAM.

Feature	Conventional PAM	SMP-PAM	Improvement
Stiffness Range	Fixed (0–0.5 MPa)	10 MPa–1.5 GPa	3000×
Deformation Modes	Single (bending/extension)	Multiple	+100%
Self-locking	No	Yes	New capability

Table 2
Printing Parameters.

Parameter Category	Specific Parameter	Set Value
Equipment and Materials	Printer Model	Bamboo Lab H2D
	Print Material	SMP-PLA
	Material Glass Transition Temperature	85 °C ± 5 °C
Temperature Parameters	Nozzle Temperature	220 °C
	Heated Bed Temperature	55 °C
Speed Parameters	Print Speed	200 mm/s
	Initial Layer Speed	50 mm/s
Structural Parameters	Layer Height	0.2 mm
	Perimeter Count	2
	Infill Density	100%
	Infill Pattern	Straight line
Other Parameters	Build Plate Adhesion	None
	Cooling Fan	Close

achieved through spiral shape memory polymer fibers, which exhibit variable contraction properties in McKibben artificial muscles, and demonstrate enhanced gripping capabilities. Multiple grip tests have shown that the variable stiffness soft gripper can grip objects of various shapes (40.0 mm 190 mm, 4.75 times) and materials, supporting weights of up to 650 grams. This provides an effective solution for the complex demands of soft robot applications [26].

In this study, we present a novel variable-curvature McKibben PAM with tunable stiffness by utilizing the temperature-dependent stiffness properties of shape-memory polymers (SMPs) in conjunction with 3D printing technology. Our design substitutes conventional hyperelastic tubes and elastic constraint beam in bending-type McKibben actuators with 3D-printed SMP tubes. These SMP tubes exhibit hyperelastic behavior at elevated temperatures, facilitating deformation functionality because their temperature-dependent stiffness variation allows for adjustable bending curvature. Additionally, the SMP tube's stiffness increases dramatically at low temperatures, resulting in a pressure-independent self-locking mechanism (see Table 1).

The research presented here introduces a nonlinear model tailored for the proposed PAM and performs simulation analyses using the SMP hyperelastic framework. The simulation results are rigorously validated against experimental data. By integrating our approach with current printable structure designs, the model demonstrates significant stiffness variation across temperatures and highlights the flexibility of 4D additive manufacturing. This adaptability leads to exceptional programmability within the McKibben PAM. Consequently, a single actuator can achieve multiple deformation modes, thereby significantly enhanced design versatility and broadening potential applications in field of soft robotics.

2. Design and manufacturing

The bending-type McKibben PAM is made up of three primary components: an inner bladder, an outer braided tube, and a constraint beam. Upon pressurization, the inner bladder and braided tube push the structure to expand along its axis. However, the constraint beam, positioned off-center, limits this axial deformation on one side. As a result, the whole system bends to adapt to the uneven deformation.

Achieving desired deformation in PAMs demands particular material characteristics for their components. In bending PAMs, bladder inflation serves as the main actuation mechanism, which requires the bladder material to possess hyperelastic properties. Simultaneously, the constraint beam significantly influences bending deformation and must have a flexural stiffness that is considerably lower than its tensile stiffness.

We developed a completely 3D-printed SMP-PAM by integrating both the bladder and constraint beam into a unified SMP structure. (Fig. 1). The SMP demonstrates hyperelastic properties at high temperatures, allowing for significant tube deformations, and exhibits high rigidity at low temperatures, limiting deformation primarily to bending modes. The SMP-PAM comprises two functional elements: a monolithic SMP tube and a braided tube. As shown in the cross-section, the cylindrical section serves the role of a traditional bladder, whereas the protruding square features fulfill the function of the constraint beam.

We opted for SMP-PLA as our printing material due to its superb processability and impressive mechanical strength. This biocompatible material is ideal for implants and wearable devices since it is non-toxic and free of harmful effects. Furthermore, it is entirely biodegradable, breaking down into carbon dioxide and water in natural environments, thus promoting environmental sustainability. Utilizing fused deposition modeling (FDM) technology, the structures were crafted via a layer-by-layer deposition of molten material. This method offers the advantages of rapid prototyping and low production costs. FDM is particularly apt for creating small structural components, achieving a printing precision of approximately 0.2 mm, which fulfills all the requirements for PAM fabrication in this study (see Table 2).

Through the precise regulation of temperature and working pressure, we successfully modulated both the bending angles and load-bearing capacity of the SMP-PAM. In our experimental setup, we used environmental heating to thermally activate the pneumatic muscle, with an air compressor supplying pressurized gas at ambient temperature. This setup, based on basic heat conduction principles, created a transverse thermal gradient across the printed structure's cross-section, resulting in higher exterior temperatures compared to the interior. At a constant pressure, three distinct deformation modes were observed as the heating temperature increased.

The SMP-PAM demonstrates three distinct thermo-mechanical response regimes based on the temperature distribution across its cross-section:

(1) Rigid-loading regime: When the entire cross-section remains below the glass transition temperature (T_g) of the SMP, the structure retains high stiffness with minimal deformation, showcasing optimal load-bearing capacity.

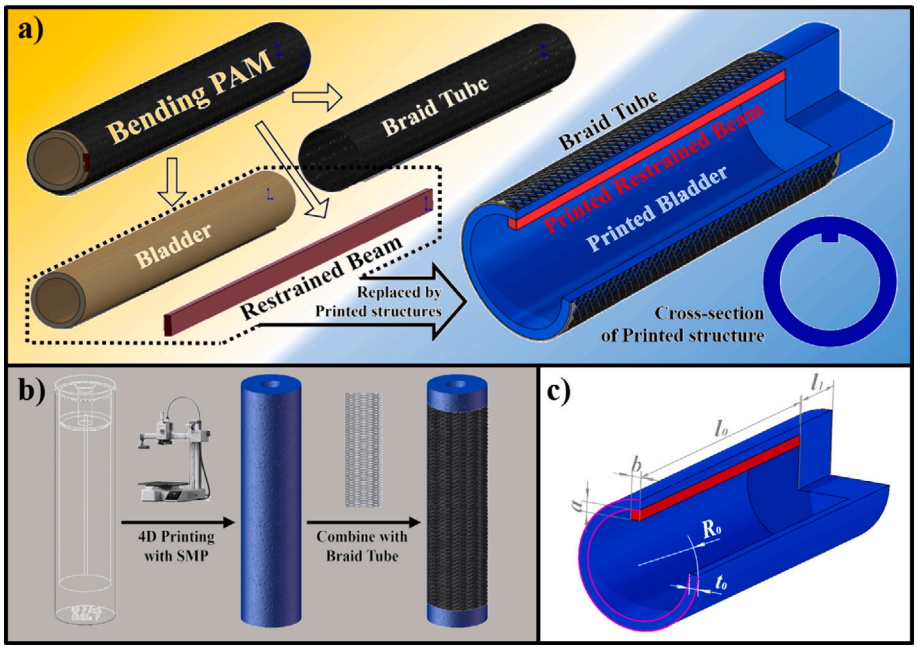

Fig. 1. Design concept of Printing Bending Pneumatic Artificial Muscles. (a)Schematic diagram of printing structure replacement. (b) Printing Manufacturing Process of SMP-PAM. (c) Geometric parameters used for manufacturing and experimentation.

Table 3
Pneumatic artificial muscle parameters for experimental and simulation analysis.

Structure parameters	Value
Initial weaving angle α_0 (°)	14
Outer diameter of the printing structure R_0 (mm)	9.5
Printing structural wall thickness t_0 (mm)	1.25
Thickness of printed constraint beam a (mm)	1.25
Width of printed constraint beam b (mm)	3
Length of deformation area l_0 (mm)	50
Length of single-sided structural area l_1 (mm)	10

(2) Controlled-bending regime: In this regime, the cylindrical section surpasses T_g while the constraint regions remain below it. The activated SMP areas exhibit hyperelastic behavior, and the SMP-PAM exhibits mechanical properties similar to traditional bending-type PAMs, achieving significant bending curvature and output torque.

(3) Axial-extension regime: At temperatures uniformly above T_g, the entire structure becomes hyperelastic, rendering the constraint beam ineffective. The SMP-PAM demonstrates minimal bending curvature, closely mirroring the behavior of extension-type PAMs. Notably, temperature adjustments can be dynamically applied during operation. Instantly cooling the system below T_g at any stage of deformation leads to immediate stiffness recovery and motion locking. Reheating then allows the system to revert to its original deformation mode. Through iterative testing, we have successfully optimized the fabrication parameters, detailed in Table 3.

3. Modeling

This section presents a comprehensive analysis of the printed pneumatic artificial muscle's (PAM) kinematics and output bending moment [27,28]. We established the relationship between the initial braiding angle and maximum deformation while evaluating output force and bending moment under varying temperature conditions. To facilitate theoretical calculations, the following assumptions were adopted [29,30]:

(1) The braided tube fibers possess infinite elastic modulus with negligible tensile deformation;

(2) Frictional effects between the braided tube and printed structure are disregarded;

(3) The cross-sectional envelope maintains perfect circularity during deformation;

(4) Below the glass transition temperature (T_g), the constraint beam is modeled as a bendable but inextensible elastic material with finite flexural rigidity;

(5) Above Tg, all printed structures are treated as incompressible hyperelastic materials.

This study simplifies the cross-section of pneumatic muscles during compression expansion to a perfect circle, a common engineering simplification aimed at establishing a concise analytical force–displacement relationship. In actual deformation, the cross-section tends toward an elliptical shape due to geometric constraints imposed by the woven structure. Zhou et al. noted that when establishing a model for path-dependent cross-sectional variations in 3D woven composite tubes, adopting this simplification may introduce average errors of approximately 5% to 9% in predicting critical geometric dimensions [31]. Another study on woven composite unit cell models also demonstrated that accounting for the continuous transition of fiber bundle cross-sections from circular to elliptical significantly improves geometric prediction accuracy (with errors below 4%). These studies quantitatively reveal that neglecting cross-sectional deformation introduces certain errors. However, given that the core objective of this research is to construct a theoretical framework capable of revealing overall actuation trends and stiffness regulation mechanisms, this simplification is reasonable and necessary to ensure the model's practicality and solubility.

In the model, we did not explicitly account for friction between the woven tube and the external SMP constraint structure. This simplification was primarily adopted to balance computational complexity and practicality in soft robotics mechanics modeling, as accurately characterizing distributed friction contacts in complex multiphysics-coupled models would significantly increase computational costs. Furthermore, friction coefficients are highly dependent on manufacturing processes and assembly conditions, making precise acquisition challenging. Stella et al. explicitly noted in their study of reduced-order models for soft

robot-environment interactions that model development requires balancing computational manageability with modeling accuracy [32]. Appropriate simplifications are crucial for enabling effective theoretical analysis and control design.

3.1. Mechanics model

Given the considerable complexity in deriving force equilibrium equations for three-dimensional bending deformations, we developed a nonlinear quasi-static model based on the principle of virtual work. This energy-based formulation effectively captures the coupled interactions between pneumatic input and structural mechanics, as well as their collective influence on actuation performance.

For an infinitesimal PAM segment of unit length dl, the work-energy principle establishes the fundamental relationship between the pneumatic input and the elastic energy distribution among structural components:

$$dW_{\text{in}} + dW_{\text{out}} = dU_{\text{E}} \tag{1}$$

$$W_{\text{in}} = PdV_{\text{in}} \tag{2}$$

$$W_{\text{out}} = -F_{\text{out}}ds - M_{\text{out}}d\theta \tag{3}$$

$$U_E = d(U_{\text{pr}} + U_{\text{br}}) \tag{4}$$

where P is Driver working pressure, V_{in} is internal working volume of printing structure. F_{out}, M_{out} represents the output force and torque at the end of the unit, while U_{pr} and U_{br} denotes the elastic strain energy of printed structures and braided tubes.

Under elevated temperature conditions, a non-uniform thermal distribution emerges within the printed structure. The outer cylindrical part surpasses the glass transition temperature (T_g) and displays hyperelastic characteristics, whereas the inner frame structure stays below Tg and retains its elastic properties. This thermal gradient induces differential elastic strain energy distributions during deformation, yielding the following relationship:

$$dU_{\text{pr}} = d(U_{\text{cy}} + U_{\text{f}}) \tag{5}$$

In this formulation, U_{cy} represents the elastic strain energy stored in the cylindrical portion of the printed structure, while U_{f} denotes the elastic strain energy accumulated in the constraint beams of the printed assembly.

Furthermore, the braided reinforcement fibers are modeled as perfectly rigid, exhibiting zero elastic strain energy contribution, $dU_{\text{br}} = 0$.

This analysis requires separate consideration of two operational regimes based on thermal conditions: (1) Only the cylindrical cross-section exceeds Tg, and (2) The entire cross-section surpasses T_g.

In Regime (2) - where the cylindrical portion exceeds T_g while constraint regions remain below T_g - the activated SMP domains exhibit hyperelastic behavior. Under these conditions, the SMP-PAM demonstrates mechanical responses analogous to conventional bending-type PAMs [6], achieving both significant bending curvature ($\kappa > 0.15\ \text{mm}^{-1}$) and substantial output torque ($M > 2.5$ N m).

Based on the principle of virtual work, the following relationship can be established

$$M_P = \pi P\left[(2R + 3kR^2)\frac{R}{k'} + R^3\right] \tag{6}$$

$$M_E = \frac{dU}{d\theta} = M_{\text{cy}} + M_f \tag{7}$$

$$M_{\text{out}} = M_P - M_E = \frac{dW_{\text{in}}}{d\theta} - \frac{d(U_{\text{cy}} + U_f)}{d\theta} \tag{8}$$

The bending moment system of the pneumatic driver comprises several key components: the driving bending moment (M_P) generated by internal air pressure acts as the primary actuation force. This driving moment is counteracted by multiple antagonizing moments: the elastic deformation resistance (M_E), the cylindrical printing structure's mechanical resistance (M_{cy}), and the constrained frame printing structure's resistance (M_f). The net resultant of these interacting moments determines the system's final output bending moment (M_{out}), which governs the actuator's motion characteristics.

Based on Assumption (4) stated previously, where the constraint beam is modeled as a bendable yet inextensible elastic material with finite flexural rigidity when operating below T_g, we neglect the axial strain in the printed constraint structure. Consequently, the bending moment M_f generated by the constraint structure can be expressed as:

$$M_f = \frac{dU_f}{d\theta} = E_f I_f k' = E_f I_f\left(\frac{k}{1 - kR}\right) \tag{9}$$

where I_f represents the axial bending moment of inertia of the constraint structure.

Consistent with Assumption (5) stated earlier, when the operating temperature exceeds T_g, the cylindrical printed structure is treated as an incompressible hyperelastic material. Applying the Mooney–Rivlin hyperelastic material model [33], we obtain:

$$W_{\text{cy}} = \sum_{i=0,j=0}^{i=1,j=1} C_{ij}(\bar{I}_1 - 3)^i(\bar{I}_2 - 1)^j \tag{10}$$

$$\lambda_{\text{cy},1}\lambda_{\text{cy},2}\lambda_{\text{cy},3} = 1 \tag{11}$$

where $\lambda_{\text{cy},1}$, $\lambda_{\text{cy},2}$ and $\lambda_{\text{cy},3}$ represent the axial, circumferential, and radial stretch ratios of the cylindrical printed structure.

According to the principle of virtual work, the cylindrical printed structure produces a resisting bending moment as follows:

$$M_{\text{cy}} = \frac{\mathrm{d}U_{\text{cy}}}{\mathrm{d}k}\frac{\mathrm{d}k}{\mathrm{d}\theta} = \lambda_{\text{cy},1}\left(\int_0^{A_{\text{cy}}}\frac{\mathrm{d}W_{\text{cy}}}{\mathrm{d}k}\,\mathrm{d}A\right)R_0 \tag{12}$$

$$M_E = M_{\text{cy}} + M_f = \lambda_{\text{cy},1}\left(\int_0^{A_{\text{cy}}}\frac{\mathrm{d}W_{\text{bl}}}{\mathrm{d}k}\,\mathrm{d}A\right)R_0 + E_f I_f\left(\frac{k}{1 - kR}\right) \tag{13}$$

The resultant output bending moment M_{out} can be expressed as:

$$\begin{aligned} M_{\text{out}} &= \frac{\mathrm{d}W_{\text{in}}}{\mathrm{d}\theta} - \frac{\mathrm{d}U}{\mathrm{d}\theta} = M_P - M_E \\ &= \pi P\left[(2R + 3kR^2)\frac{\mathrm{d}R}{\mathrm{d}k} + R^3\right] \\ &\quad - \left(\int_0^{A_{\text{cy}}}\frac{\mathrm{d}W_{\text{bl}}}{\mathrm{d}k}\,\mathrm{d}A\right)R_0 - E_f I_f\left(\frac{k}{1 - kR}\right) \end{aligned} \tag{14}$$

When the entire cross-section exceeds the glass transition temperature (T_g), the printed structure becomes fully hyperelastic, effectively negating the constraint beam's function. Under these conditions, the SMP-PAM demonstrates minimal bending curvature, exhibiting behavior analogous to extension-type PAMs. For this operational mode, well-established mechanical models exist to determine the radial and axial stresses in extensible pneumatic artificial muscles. Through stress integration, the actuator's output force can be derived [34].

$$\sigma_\theta = \sigma_r + 2D\left(\frac{C_{10}}{\lambda} + C_{01}\lambda\right)\frac{2r^2 - D}{r^2(r^2 - D)} \tag{15}$$

$$\sigma_z = \sigma_r + \left(2C_{10}\lambda^2 - 2C_{01}\frac{1}{\lambda^2}\right) - \frac{2C_{10}}{\lambda}\frac{r^2 - D}{r^2} + 2C_{01}\lambda\frac{r^2}{r^2 - D} \tag{16}$$

The constitutive equation for pneumatic muscles involves the following parameters: C_{10} and C_{01} represent the material constants derived from the Mooney–Rivlin hyperelastic model, D denotes an undetermined geometric constant related to the wall thickness, λ expresses the axial stretch ratio of the muscle under pressurization, while r indicates the instantaneous radial coordinate. The stress components σ_θ and σ_z correspond to the circumferential and axial stresses, respectively,

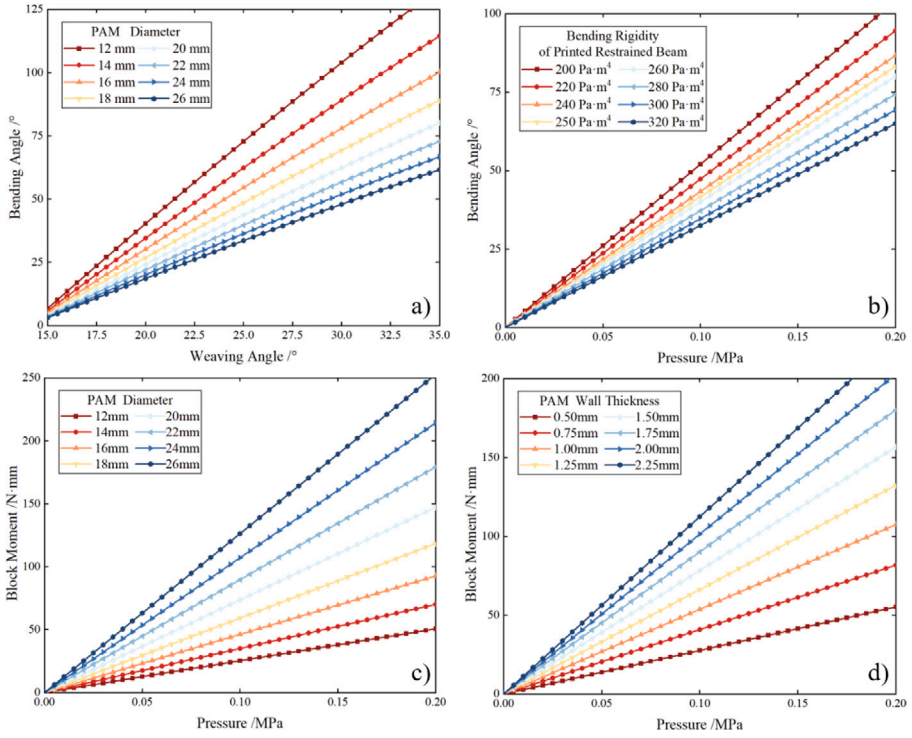

Fig. 2. Theoretically calculated result (a) Correspondence between initial weaving angle and bending angle under different diameters. (b) Correspondence between air pressure and bending angle under different constraint beam conditions. (c) Correspondence between air pressure and locking bending moment under ideal conditions of different diameters. (d) The correspondence between air pressure and locking bending moment under ideal conditions of different wall thickness.

3.2. Motion analysis

In conventional fiber-reinforced pneumatic artificial muscles (PAMs), the braided mesh is typically modeled as inextensible along the radial direction of individual fibers while remaining freely movable in other directions [35]. Under the condition of constant fiber length, varying braiding angles correspond to different cross-sectional areas and axial lengths, thereby altering the internal volume. When pressurized, the internal chamber expands to maximize its volume, resulting in either reduced cross-section with axial elongation, or expanded cross-section with axial contraction.

This fundamental mechanism enables the essential extension/contraction functionality of PAMs. Given the unique correspondence between internal volume and braiding angle, geometric analysis yields the optimal initial braiding angle (α_0) for maximum volume capacity.

$$[\cos\alpha_0(1+\varepsilon_1)]^2+[\sin\alpha_0(1+\varepsilon_2)]^2=\cos^2\alpha_0\lambda_1^2+\sin^2\alpha_0\lambda_2^2 =\cos^2\alpha+\sin^2\alpha=1 \tag{17}$$

When considering solely the braided mesh constraints, the theoretical axial output force can be expressed as:

$$F_{\text{out}}=\pi R^2(3\cos^2\alpha-1) \tag{18}$$

When $F_{\text{out}}=0$, the critical braiding angle ℵ is determined to be 54.74°.

Leveraging this fundamental characteristic, we can precisely control the actuator's extension/contraction motion by engineering the initial braiding angle, which governs the volumetric expansion behavior of the inner braided chamber. Furthermore, through the strategic incorporation of constraint mechanisms, this linear motion can be transformed into more complex deformations, including bending and helical twisting.

When the cylindrical section exceeds the glass transition temperature (T_g) while constraint regions remain below T_g, the activated SMP exhibits hyperelastic behavior, enabling the SMP-PAM to demonstrate mechanical characteristics comparable to conventional bending-type PAMs. This configuration produces:

$$\varepsilon_1=\lambda_1-1\approx k_f(1-\cos\Phi)r \tag{19}$$

The strain distribution on the PAM surface is governed by the interplay between the braiding angle and bending curvature, as expressed by:

$$\varepsilon_2=\frac{\sqrt{1-[\cos\alpha(1+\varepsilon_1)]^2}}{\sin\alpha}-1=\sin\alpha\left[k_f(1-\cos\Phi)r\right]-1 \tag{20}$$

The maximum achievable bending curvature occurs when the output bending moment $M_{\text{out}}=0$, yielding:

$$\pi P\left[(2R+3kR^2)\frac{\mathrm{d}R}{\mathrm{d}k}+R^3\right]-\left(\int_0^{A_{\text{cy}}}\frac{\mathrm{d}W_{\text{bl}}}{\mathrm{d}k}\mathrm{d}A\right)R_0=E_fI_f\left(\frac{k}{1-kR}\right) \tag{21}$$

When the entire cross-section temperature exceeds T_g, the fully activated SMP-PAM exhibits homogeneous hyperelastic behavior, effectively nullifying the constraint beam's mechanical influence. In this regime, the actuator demonstrates minimal bending curvature, behaving essentially as an extension-type PAM. The axial stretch ratio λ_1 can be determined from geometric analysis as:

$$\lambda_1=\frac{sin\alpha_0}{sin\alpha} \tag{22}$$

where α represents the initial braiding angle.

This study conducts a comprehensive parametric analysis of the bending performance through systematic computational simulations, as shown in Fig. 2. The investigation evaluates the interrelationships between the braiding angle, input pressure, free bending angle, and blocking torque under various structural parameters, including the printed structure's diameter, wall thickness, and the constraint beam's flexural rigidity. The results demonstrate that under ideal pure bending conditions of the constraint beam, the free bending angle exhibits

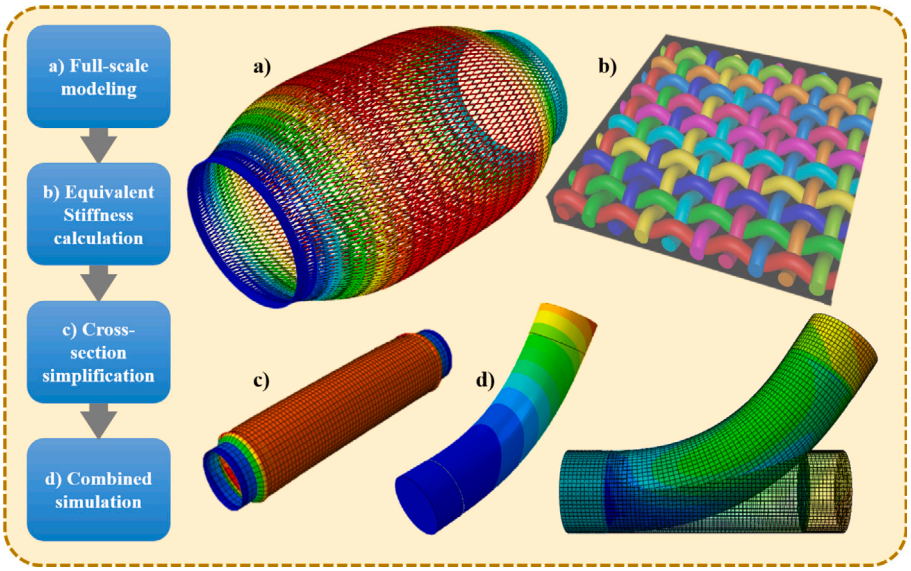

Fig. 3. ESimulation analysis approach (a) Full-scale modeling; (b) Equivalent Stiffness calculation; (c) Cross-section simplification; (d) Combined simulation.

a clear inverse correlation with the beam's bending stiffness. Furthermore, the braiding angle, diameter, and wall thickness of the printed structure collectively influence both the free bending angle and blocking torque. Specifically, structures with thicker walls and larger diameters show significantly improved pressure-to-torque conversion efficiency, enabling stronger blocking torque generation under identical input pressure conditions. The parametric studies cover the following ranges: diameter, wall thickness, and constraint beam flexural rigidity.

4. Simulation analysis

Compared to experimental validation, finite element analysis (FEA) enables rapid and cost-effective verification of deformation and motion functions in complex structures [36–38], thereby guiding design optimization and facilitating fast iterations [39–41]. In this study, we employed Abaqus/CAE to simulate the motion and deformation of the pneumatic artificial muscle (PAM) model.

The numerical approach provides detailed insights into the structural behavior under various loading conditions while significantly reducing development time and material costs associated with physical prototyping. This computational methodology allows for efficient parametric studies and performance prediction before manufacturing actual prototypes.

The primary challenge in simulating braided pneumatic artificial muscles is accurately characterizing the deformation behavior of the braided tube. Directly modeling the entire braided structure is computationally demanding due to the numerous surface contacts between the sleeve and inner components, leading to high computational costs and difficulties in achieving convergence. To overcome this, we propose a multi-stage modeling approach:

1. Develop a full-scale model of the braided tube to determine its tensile and shear stiffness.

2. Use these findings to create a simplified equivalent cross-section model.

3. Integrate this equivalent representation with the internal elastomer components in a coupled simulation.

This optimized computational method, as shown in the accompanying diagram, reduces solving time by approximately 70% while maintaining over 90% accuracy compared to experimental data (see Fig. 3).

The external sleeve consists of a nylon braided tube, modeled as an anisotropic material whose tensile and shear stiffness properties were derived from full-scale simulations. The principal stress direction aligns with the initial braiding angle.

The internal printed structure is fabricated from shape-memory polymer (SMP). At temperatures below the glass transition point (T_g), the SMP behaves as a conventional elastic material, with a Young's modulus of 1500 MPa as determined through tensile testing.

Dynamic mechanical analysis (DMA) measures the time-dependent stress or strain response of polymeric materials under oscillatory loading while varying temperature [42]. This method characterizes the viscoelastic properties of materials over defined temperature ranges. In this study, we fabricated PLA shape-memory polymer (SMP) specimens compatible with DMA tensile testing. The experiments were conducted under the following conditions: Temperature range: 25 ℃ (room temperature) to 150 ℃; Heating rate: 2 ℃/min; Loading frequency: 1 Hz (tensile mode). The results identified the glass transition temperature at 86 ℃, a critical parameter for SMP actuation performance.

The high-temperature deformation behavior was modeled using the Mooney–Rivlin hyperelastic formulation, which outperforms the Neo-Hookean model in capturing nonlinear large deformations through higher-order strain invariants. Material parameters (C_{10} = 0.163 MPa, C_{01} = $3.6 \times 10^{-3} MPa$) were calibrated via least-squares fitting to uniaxial tensile test data [33]. Finite element simulations implementing these parameters with fixed-free boundary conditions and 0.2 MPa internal pressure generated the stress/displacement distributions shown in Fig. 4, demonstrating the model's capability to predict complex deformations under thermomechanical loading.

5. Experiment and results

5.1. Working temperature calibration

The deformation behavior of the designed SMP-PAM is governed by two external stimuli: pneumatic pressure required for structural deformation and temperature, which critically determines material properties. In this study, temperature directly modulates structural stiffness and deformation modes, making its precise control essential for SMP-PAM performance.

To investigate thermal effects on bending curvature, we characterized temperature distribution using a UT325F thermometer with K-type thermocouples, measuring four key locations (see figure):

T_1: Ambient heating temperature

T_2: Actuator outer surface

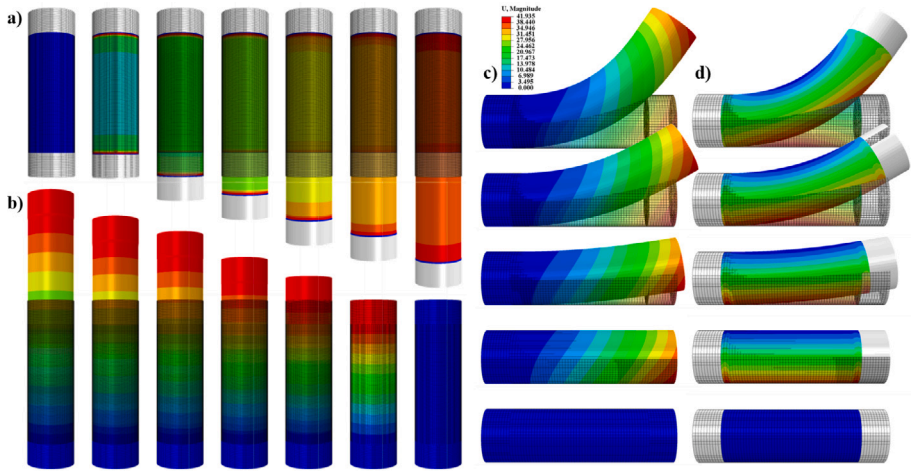

Fig. 4. Simulation results (a) Stress distribution in the state of elongation deformation; (b) Deformation distribution of elongation deformation state; (c) Deformation distribution of bending deformation state; (d) Stress distribution in the state of bending deformation.

T_3: Actuator inner surface

T_4: Constraint structure interior

And three distinct thermo-mechanical regimes were identified:

1. Rigid-loading regime (T_3, $T_4 < T_g$): High stiffness enables superior load-bearing but negligible deformation.

2. Controlled-bending regime ($T_3 > T_g$, $T_4 < T_g$): SMP exhibits hyperelasticity, producing large bending curvature and output torque akin to conventional bending PAMs.

3. Axial-extension regime (T_3, $T_4 > T_g$): Near-loss of constraints yields minimal curvature, resembling extension-type PAMs.

This study comprehensively reveals the response characteristics of mode switching through time-series data of temperature distribution and controlled experiments on heating duration. Under ambient heating conditions, the response time is primarily determined by heating duration and the heat transfer process, effectively regulated by heat source power, heating duration, and ambient temperature. When the heat transfer coefficient, heat source power, and ambient temperature are fixed, the response time in this study is predominantly governed by heating duration.

As shown in Fig. 5(b), after heating for 320 s, T_3 rises above the glass transition temperature (T_g). At this point, heat rapidly transfers from the ambient environment (T_1) to the surface of the SMP layer (T_2, T_3), causing it to soften quickly. Meanwhile, the interior of the constrained beam (T_4) remains rigid due to thermal inertia, leading to bending deformation of the SMP-PAM tube. Maintaining the ambient temperature and continuing heating for 30 s allows heat to continue diffusing inward until the constrained structure softens. At this point, the bending constraint weakens, and the actuator transitions to axial extension. T_4 also rises above the T_g, causing the SMP-PAM tube to undergo elongation deformation. After heating ceases, the system recovers its rigid mode during natural cooling, a process taking approximately 60 s.

By setting different heating durations, the timing and sequence of mode transitions can be precisely controlled. Closed-loop temperature feedback based on real-time data from T_2, T_3, and T_4 also enables dynamic compensation and control of response times. This mechanism provides a controllable deformation timing foundation for time-critical tasks in practical applications, such as sequential grasping and adaptive gait switching.

5.2. Free bending test

The term “free bending” refers to the bending deformation behavior of the pneumatic artificial muscle (PAM) when subjected to pneumatic pressure in the absence of external loads. In this study, the SMP-PAM exhibits two primary deformation modes: bending and elongation. While the elongation behavior is similar to that of conventional McKibben PAMs and has been extensively studied in prior works, the current investigation focuses exclusively on characterizing the free bending deformation of the newly designed SMP-PAM.

This targeted approach allows for a comprehensive analysis of the unique bending performance enabled by the shape-memory polymer (SMP) and structural design. By isolating the bending behavior, we systematically evaluate how temperature-dependent stiffness modulation and constraint mechanisms influence the actuator’s curvature and output capabilities under varying pressure inputs.

The free bending tests provide essential baseline data for understanding the SMP-PAM’s actuation mechanics, which will later inform applications requiring controlled bending motions in soft robotics and biomedical devices. This focused methodology complements existing research on McKibben-type elongation while advancing knowledge of thermally programmable bending actuators.

The deformation testing system comprised a 6L MZB air compressor with dual-stage pressure regulation (primary: 0–1 MPa analog; secondary precision: 0.005–0.2 MPa, ±0.001 MPa) and filtration, coupled with a temperature-controlled chamber for SMP activation. Under 0.200 MPa pressure, the SMP-PAM (fabricated per Section 2 parameters) exhibited maximum deformation of 40.622 mm with a 110.4° free bending angle, demonstrating its programmable bending capability through combined thermal-pneumatic actuation [43].Repeat the experiment five times and take the average. This integrated setup enabled precise quantification of the actuator’s performance while maintaining experimental repeatability (see Fig. 6).

5.3. Uniform bending moment loading test and characterization

To comprehensively characterize the mechanical properties of the pneumatic artificial muscle (PAM) and elucidate the respective roles of the elastic bladder and flexible frame, quasi-static tests were conducted at varying temperatures. A four-point bending fixture mounted on a Zwick universal testing machine was employed to apply moment loads, with the resulting bending moments calculated through mechanical analysis.

The SMP-PAM was mechanically characterized under four distinct thermomechanical states: (1) pressurized bending when heated to $T_3 > T_g$ while $T_4 < T_g$, (2) pressurized extension when both $T_3 and T_4 > T_g$, (3) bend-locked state after cooling, and (4) extension-locked state after cooling. Key results demonstrated:

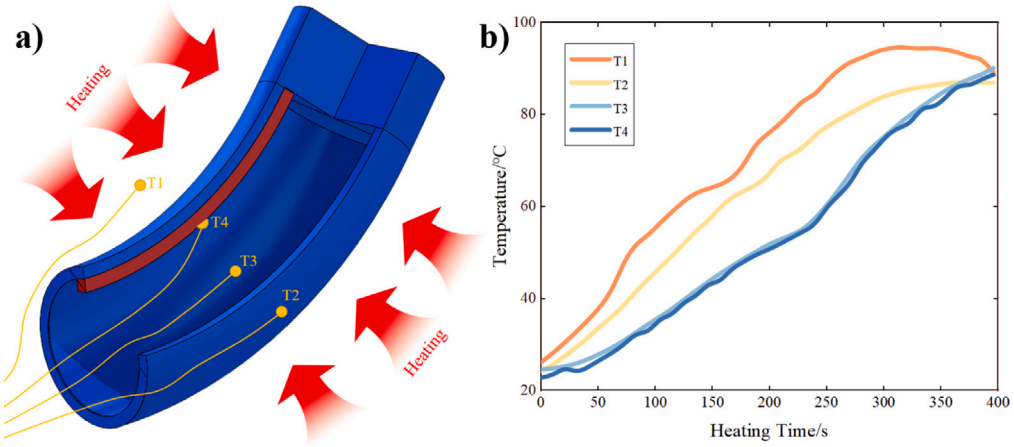

Fig. 5. Calibration of SMP-PAM Operating Temperature (a) Heating Method and Thermocouple Distribution Diagram (b) Heating Process Temperature Rise Curve at Different Calibration Points.

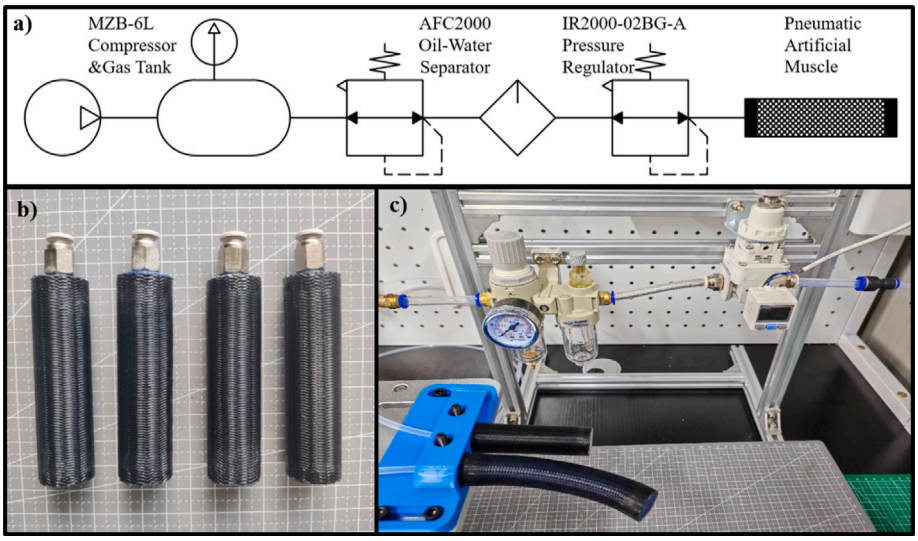

Fig. 6. Design of pneumatic system for PAM drive (a) Pneumatic system design flowchart (b) SMP-PAM physical sample prepared (c) Overall physical diagram of pneumatic drive system.

(1) The locked states achieved high stiffness ($E \approx$ 1.2-1.5 GPa) dominated by intrinsic material properties.

(2) Heated extension showed minimal bending resistance ($\kappa <$ 0.05 mm^{-1});

(3) Heated bending produced intermediate stiffness with a maximum output moment of 150 N mm - comparable to conventional PAMs.

This quantified the actuator's programmable stiffness range ($\Delta E >$ 1 GPa) and validated its dual-mode functionality (see Fig. 7).

5.4. Shape recovery rate experiment

The shape-memory polymer (SMP) in the designed SMP-PAM showcases distinctive shape recovery properties, allowing for the programmable locking and reactivation of deformation modes. During its operation, a swift cooling process below the glass transition temperature (T_g) initiates a rapid recovery of stiffness, with an increase in E by more than 300%, effectively locking the motion by suppressing the hyperelasticity of the printed structure. When reheated above T_g, the original deformation behavior is reinstated, illustrating completely reversible shape-memory cycles [44].

The SMP-PAM demonstrated exceptional shape-memory performance, achieving 97.3% axial and 92.9% radial recovery ratios through controlled thermo-pneumatic cycling (heating > 86 ℃ with 0.20 MPa pressure, rapid cooling < 86 ℃, then reheating). The minor 7.1% radial strain retention reflects minimal viscoelastic relaxation during quenching, validating robust geometric restoration capability. This quantitative assessment (5 test cycles) confirms reliable shape recovery under repeated actuation, with performance metrics suitable for applications requiring precise shape programming.

5.5. Thermal-mechanical cycling test

The performance degradation of shape memory polymers (SMPs) under repeated thermal-mechanical loading — such as reduced shape recovery rates, stiffness decay, and material aging — constitutes a core consideration for their engineering applications. To quantitatively evaluate the durability of the SMP-PAM composite actuator proposed in this study, systematic thermomechanical cycling tests were designed and conducted in this section. The experiments aimed to obtain evolution data for key performance parameters of the actuator through finite-cycle testing at the specimen level. This validated its functional stability during short-to-medium-term operation and provided early insights for understanding long-term behavior.

The tests were conducted on a self-built experimental platform. This platform integrates temperature control, pneumatic actuation, and

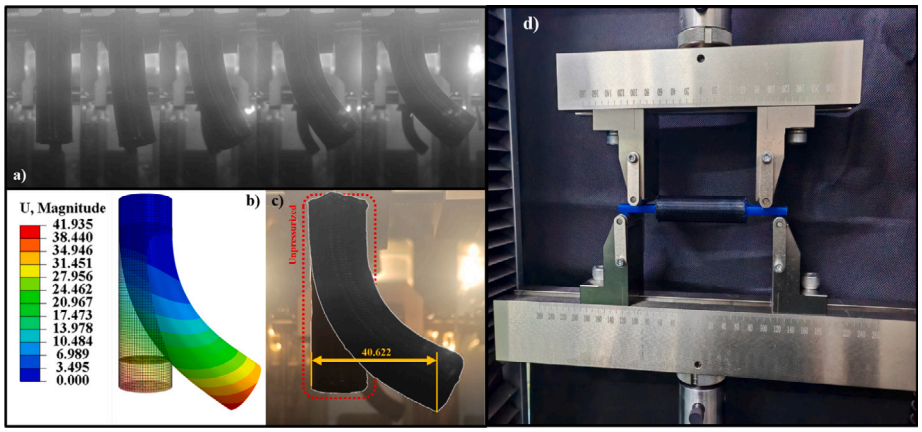

Fig. 7. (a) PAM bending deformation process (b) simulation deformation results (c) experimental results (d) bending experimental fixture.

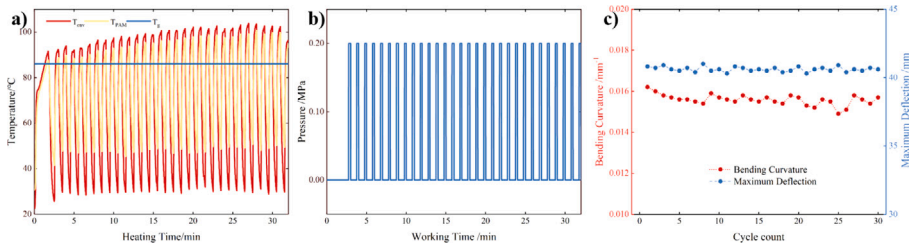

Fig. 8. Thermal-Mechanical Cycling Test (a) Temperature cycles; (b) Pressure cycles; (c) Bending curvature and maximum deflection; (d) Actual images under different cycles.

a multi-parameter synchronous acquisition system. The temperature control unit comprises a programmable temperature controller, an oven, and K-type thermocouples, ensuring the SMP section is heated uniformly and precisely to the target temperature. The pneumatic actuation unit consists of a precision air source, proportional valves, and controllers. The test subjects were SMP-PAM actuator samples (n=3) fabricated for this study. Each specimen undergoes an identical test sequence to ensure reproducibility and statistical significance: "heating for softening - pneumatic actuation to target bending angle - cooling for locking - heating for reset" (see Fig. 8).

Test results clearly reveal the performance evolution of the SMP-PAM actuator under thermomechanical cycling. All performance parameters exhibit a similar two-stage pattern of "initial adjustment followed by long-term stability". Bending curvature consistently fluctuates randomly within the strictly controlled set range. The average maximum deflection stabilizes at 40.6, with fluctuations limited to ±1.2. No observable significant degradation in the actuator's core functionality occurred throughout the test cycle.

The observed "two-stage" evolution aligns closely with the material science principles of SMPs. The initial performance adjustment primarily stems from the SMP molecular chain network releasing internal stresses and reconfiguring during the first multiple cycles to reach a thermodynamic metastable state [45]. This universal phenomenon and its underlying two-phase network mechanism have been extensively studied and validated by theoretical models [46]. Seo et al. reported a biomass-based artificial muscle fiber based on polylactic acid (PLA), where the optimized SMP-PLA conjugated fiber maintained a shape recovery rate exceeding 98.3% after 50 consecutive cycles [47]. Subsequent long-term stability tests demonstrated the superior fatigue resistance of the SMP-PLA material system and the "pneumatic drive-SMP constraint" composite structure employed in this design. Research also indicates that rational material design can effectively enhance the cyclic life of SMPs [48,49], pointing the way for future material optimization of this actuator.

Although this 30-cycle test did not achieve the ultra-long lifespan required for certain extreme applications, the results demonstrate the actuator's high functional reliability in short-to-medium-term tasks with limited cycles. The stability of performance parameters provides a credible data foundation for predicting its long-term behavior. Compared to traditional pure pneumatic artificial muscles (PAM), this actuator potentially reduces fatigue in pneumatic components due to the SMP bearing the primary structural load in the rigid state. This constitutes a potential durability advantage warranting direct comparative studies in the future.

5.6. Proof of concept

To validate the application value of the multimodal soft actuator proposed in this paper, we designed and fabricated a prototype three-finger adaptive soft gripper. The gripper employs three actuators as finger drivers, integrated into a monolithic base with a 120-degree circumferential symmetrical layout. Without requiring complex sensing or control algorithms, the gripper can switch between two modes: gently grasping fragile items and firmly holding heavy objects.

Within modeling software, the gripper base and pneumatic interface underwent lightweight and integrated design. Installation tilt angles and internally integrated independent pneumatic channels were engineered to ensure coordinated control of all fingers. All structural components were printed using FDM technology. The core "finger" parts were directly fabricated from SMP-PLA material, strictly adhering to the printing parameters outlined in Chapter 2 to guarantee their shape memory and stiffness switching performance. The support base was printed using rigid PLA to maintain overall stability. After fabrication, woven tubing, pneumatic connectors, and other components were

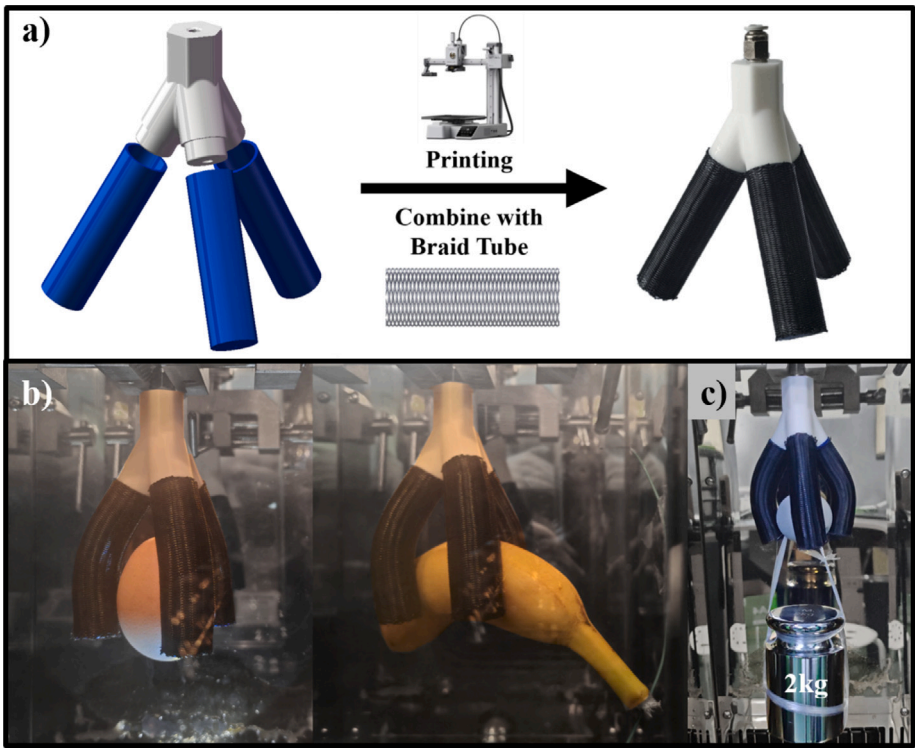

Fig. 9. Three-Finger Adaptive Soft Gripper (a) Conceptual Design and Fabrication (b) Handling Fragile/Irregular Objects in Low-Stiffness Mode (c) Supporting 2 kg Weight in High-Stiffness Mode.

Table 4
The SMP-PAM parameter comparison of the theoretical results, simulations and experiments.

Performance parameter	Theoretical-Value	results Error	Simulation-Value	results Error	Experiments Value
Block moment (N mm)	157	11.3%	169	19.9%	141 ± 6
Bending curvature (mm^{-1})	0.0127	18.2%	0.0143	8.33%	0.0156 ± 0.009
Radial shrinkage rate (%)	38.6	4.93%	39.0	3.94%	40.6 ± 2.7
Radial displacement (mm)	28.2	13.8%	34.9	6.73%	32.7 ± 1.1
Maximum deflection (mm)	45.3	11.6%	41.9	3.2%	40.6 ± 1.2
Axial shape recovery rate (%)	/	/	100	2.7%	97.3 ± 2.0
Radial shape recovery rate (%)	/	/	100	7.1%	92.9 ± 2.1

integrated according to the design, assembling the complete gripper system.

The gripper features two preset operational logics: (1) Adaptive Envelope Mode: Inflates the fingers while the SMP is in its softened state (low stiffness), enabling gentle bending to conform to object surfaces; (2) Powerful Grasping Mode: First heats and softens the fingers to preform them to a curvature matching the target object, then cools the SMP to lock it in a high-stiffness state before applying pneumatic pressure to generate strong clamping force (see Fig. 9).

Its unique advantages in scenarios requiring safe interaction and adaptive manipulation have been validated. Experiments demonstrate the gripper's reliable handling of diverse objects ranging from eggs and irregularly shaped fruits to moderately weighted tool components. Its adjustable stiffness directly addresses the pain points of traditional rigid grippers causing object damage and conventional soft grippers lacking sufficient load capacity. This provides a clear technological prototype for applications in medical rehabilitation, service industries, and advanced manufacturing.

5.7. Error analysis

This section conducts an attribution analysis of systematic errors identified in the comparison of theoretical, simulation, and experimental data presented in Table 4. The existing errors primarily originate from the following three levels:

The hyperelastic constitutive model employed in simulations represents an idealized characterization of SMP-PLA's nonlinear, rate-dependent, and path-dependent behavior under complex thermal-mechanical cycling. This model struggles to fully capture the material's significant modulus changes near the glass transition region, as well as the mechanical hysteresis effects arising from molecular chain orientation and relaxation. This simplification inevitably leads to predictable

computational deviations when predicting torque output dependent on the material's instantaneous stiffness.

The simulation environment assumes ideal fixed constraints and frictionless contact. However, the experimental system features micrometer-scale assembly gaps, micro-slip between connectors, and distributed friction at the interface between the braided tube and the SMP constraint structure. These unmodeled energy dissipation mechanisms effectively reduce force transmission efficiency, causing experimentally measured output parameters to fall below the ideal values predicted by simulation.

The FDM-based 3D printing process introduces inherent manufacturing errors, including non-uniform interlayer bonding strength, material anisotropy due to micrometer-scale layer striations, and cross-sectional dimensional variations caused by nozzle extrusion fluctuations. These manufacturing tolerances result in local stiffness distributions within the actual SMP components that differ from the homogeneous, ideal geometric model used in simulations, directly affecting their mechanical response to external loads.

Existing errors primarily stem from three systemic factors prevalent in engineering research and difficult to eliminate entirely: model simplification, boundary idealization, and manufacturing tolerances. However, the highly consistent qualitative trends and variation patterns observed across all operating modes in theory, simulation, and experiment demonstrate the reliability of the theoretical framework established herein for revealing intrinsic physical mechanisms and predicting system behavior.

6. Discussion

This study introduces the design and fabrication of a novel pneumatic artificial muscle (PAM) that integrates both stiffness-tunable and curvature-tunable capabilities. While conventional braided PAMs have demonstrated certain flexible characteristics, their fixed stiffness properties inherently limit deformation performance and practical applications. Our innovative approach addresses this fundamental constraint by incorporating variable stiffness mechanisms, achieving remarkable improvements in both deformability and load-bearing capacity.

The current study utilizes the thermoresponsive characteristics of shape memory polymers (SMPs) alongside cutting-edge 4D printing technology to create a next-generation bending-type McKibben pneumatic artificial muscle (PAM). The SMP material demonstrates a significant stiffness change ($\Delta E > 1$ GPa) at its glass transition temperature ($T_g = 86$ ℃, as measured by dynamic mechanical analysis), opening up fundamentally new possibilities for actuation.

This study develops a comprehensive theoretical framework to characterize the SMP-PAM's thermomechanical behavior through nonlinear quasi-static modeling based on the principle of virtual work. The model incorporates three critical aspects of actuator performance.

The experimental results demonstrate the SMP-PAM's exceptional multifunctionality, achieving three distinct operational modes through thermal control: bending-dominant (110.4° maximum bending angle at partial activation), extension-dominant (35% axial strain at full activation), and rigid-locked modes (1.5 GPa stiffness). Dynamic mechanical analysis has confirmed the thermoresponsive behavior, demonstrating a glass transition at 86 ℃ and a dramatic 300-fold change in stiffness, shifting from 1.5 GPa to 8 MPa. Performance metrics highlight significant advancements over traditional PAMs, such as a 23% increase in bending range and an exceptional shape memory capability, achieving 97.3% recovery. These quantified results establish new benchmarks for soft actuators, combining pneumatic power with SMP's tunable properties to enable adaptive robotic systems.

In summary, this study proposes a novel pneumatic artificial muscle (PAM) with tunable stiffness and curvature through comprehensive theoretical analysis, simulation, and experimental validation, demonstrating its broad application potential in soft robotics. The research not only provides innovative design concepts for PAMs but also establishes a foundation for future advancements in soft robotic technologies. By incorporating variable-stiffness materials and 4D printing techniques, we have successfully achieved multifunctionality and high adaptability in the PAM, significantly expanding its potential applications in complex environments.

However, the long-term stability and durability of PAM have not been fully validated, and further long-term testing is needed. There is relatively little discussion on the control strategy of PAM in research, and there is a lack of in-depth analysis on its adaptability in complex environments. Although a nonlinear model has been established, the complexity of the model may make it difficult to implement in practical applications, and further simplification and optimization are needed.

In the future, more types of variable stiffness materials can be explored to enrich the design choices of PAM and enhance its adaptability and functionality. At the same time, by combining artificial intelligence technology, an intelligent control system is developed to achieve adaptive control of PAM in dynamic environments. Explore the combination application of PAM with other types of flexible actuators to form more complex and multifunctional soft robot systems. Further research the application of PAM in fields such as healthcare, services, and precision manufacturing, and promote its commercialization process.

CRediT authorship contribution statement

Zhengyue Li: Writing – review & editing, Writing – original draft, Visualization, Formal analysis, Conceptualization. **Jian Sun:** Writing – review & editing, Writing – original draft, Visualization, Methodology, Conceptualization. **Yanju Liu:** Writing – original draft, Supervision, Project administration, Methodology, Conceptualization. **Jinsong Leng:** Writing – original draft, Project administration.

Declaration of competing interest

The authors declare that they have no known competing financial interests or personal relationships that could have appeared to influence the work reported in this paper.

Acknowledgments

This work was supported by the National Natural Science Foundation of China (General Program)(11802076).

Data availability

Data will be made available on request.

References

[1] El-Atab N, Mishra RB, Al-Modaf F, Joharji L, Alsharif AA, Alamoudi H, Diaz M, Qaiser N, Hussain MM. Soft actuators for soft robotic applications: A review. Advanced Intell Syst 2020;2(10):2000128. http://dx.doi.org/10.1002/aisy.202000128.

[2] Sarker A, Ul Islam T, Islam MR. A review on recent trends of bioinspired soft robotics: Actuators, control methods, materials selection, sensors, challenges, and future prospects. Advanced Intell Syst 2024. http://dx.doi.org/10.1002/aisy.202400414.

[3] Scalet G. Two-way and multiple-way shape memory polymers for soft robotics: An overview. Actuators 2020;9(1):10. http://dx.doi.org/10.3390/act9010010.

[4] Koizumi S, Kurumaya S, Nabae H, Endo G, Suzumori K. Recurrent braiding of thin McKibben muscles to overcome their limitation of contraction. Soft Robotics 2020;7(2):251–8. http://dx.doi.org/10.1089/soro.2019.0022.

[5] Salahuddin B, Warren H, Spinks GM. A comprehensive test method for measuring actuation performance of McKibben artificial muscles. Smart Mater Struct. 2021;30(4):045016. http://dx.doi.org/10.1088/1361-665x/abea01.

[6] Guan Q, Sun J, Liu Y, Wereley NM, Leng J. Novel bending and helical extensile/contractile pneumatic artificial muscles inspired by elephant trunk. Soft Robotics 2020;7(5):597–614. http://dx.doi.org/10.1089/soro.2019.0079.

[7] Dzahir M, Yamamoto S-i. Recent trends in lower-limb robotic rehabilitation orthosis: Control scheme and strategy for pneumatic muscle actuated gait trainers. Robotics 2014;3(2):120–48. http://dx.doi.org/10.3390/robotics3020120.

[8] Al-Fahaam H, Davis S, Nefti-Meziani S. The design and mathematical modelling of novel extensor bending pneumatic artificial muscles (EBPAMs) for soft exoskeletons. Robotics Auton Syst 2018;99:63–74. http://dx.doi.org/10.1016/j.robot.2017.10.010.
[9] Köktaş H, Kanber B. Mechanical Design and Finite Element Analysis of a Pneumatic Artificial Muscle Powered Lower Limb Exoskeleton.
[10] Wirekoh J, Park Y-L. Design of flat pneumatic artificial muscles. Smart Mater Struct 2017;26(3):035009. http://dx.doi.org/10.1088/1361-665x/aa5496.
[11] Al-Mayahi W, Al-Fahaam H. A review of design and modeling of pneumatic artificial muscle. Iraqi J Electr Electron Eng 2024;20(1):122–36. http://dx.doi.org/10.37917/ijeee.20.1.13.
[12] Tschiersky M, Hekman EEG, Brouwer DM, Herder JL, Suzumori K. A compact McKibben muscle based bending actuator for close-to-body application in assistive wearable robots. IEEE Robot Autom Lett 2020;5(2):3042–9. http://dx.doi.org/10.1109/lra.2020.2975732.
[13] Hu Y, Wang L, Li J, Yang Y, Zhao G, Liu Y, Huang X, Wu P, Zhang B, Jiao Y, Wu M, Jia S, Zhang Q, Xu G, Shi R, Li D, Li Y, Peng Z, Yu X. Thin, soft, skin-integrated electronics for real-time and wireless detection of uric acid in sweat. Int J Smart Nano Mater 2023;14(4):406–19. http://dx.doi.org/10.1080/19475411.2023.2236997.
[14] Jamil B, Oh N, Lee J-G, Lee H, Rodrigue H. A review and comparison of linear pneumatic artificial muscles. Int J Precis Eng Manufacturing-Green Technol 2023. http://dx.doi.org/10.1007/s40684-023-00531-6.
[15] Xiang C, Guo J, Chen Y, Hao L, Davis S. Development of a SMA-fishing-line-McKibben bending actuator. IEEE Access 2018;6:27183–9. http://dx.doi.org/10.1109/access.2018.2830314.
[16] Tmdu. Modeling and control of McKibben artificial muscle robot actuators. IEEE Control Syst Mag 2000. http://dx.doi.org/10.1109/37.845788.
[17] Tawk C, Alici G. A review of 3D-printable soft pneumatic actuators and sensors: Research challenges and opportunities. Adv Intell Syst 2021;3(6):2000223. http://dx.doi.org/10.1002/aisy.202000223.
[18] Leng J, Lan X, Liu Y, Du S. Shape-memory polymers and their composites: Stimulus methods and applications. Prog Mater Sci 2011;56(7):1077–135. http://dx.doi.org/10.1016/j.pmatsci.2011.03.001.
[19] Chen Y, Chen C, Rehman HU, Zheng X, Li H, Liu H, Hedenqvist MS. Shape-memory polymeric artificial muscles: Mechanisms, applications and challenges. Molecules 2020;25(18):4246. http://dx.doi.org/10.3390/molecules25184246.
[20] Liu J, Wei J, Zhang G, Wang S, Zuo S. Pneumatic soft arm based on spiral balloon weaving and shape memory polymer backbone. J Mech Des 2019;141(8). http://dx.doi.org/10.1115/1.4042618.
[21] Takashima K, Rossiter J, Mukai T. Development of a McKibben artificial muscle using a shape-memory polymer. In: Behavior and mechanics of multifunctional materials and composites 2010. SPIE; 2010, http://dx.doi.org/10.1117/12.847229.
[22] Takashima K, Noritsugu T, Rossiter J, Guo S, Mukai T. Curved type pneumatic artificial rubber muscle using shape-memory polymer. J Robot Mechatronics 2012;24(3):472–9. http://dx.doi.org/10.20965/jrm.2012.p0472.
[23] Takashima K, Rossiter J, Mukai T. McKibben artificial muscle using shape-memory polymer. Sensors Actuators A: Phys 2010;164(1–2):116–24. http://dx.doi.org/10.1016/j.sna.2010.09.010.
[24] Takashima K, Sugitani K, Morimoto N, Sakaguchi S, Noritsugu T, Mukai T. Pneumatic artificial rubber muscle using shape-memory polymer sheet with embedded electrical heating wire. Smart Mater Struct 2014;23(12):125005. http://dx.doi.org/10.1088/0964-1726/23/12/125005.
[25] Takashima K, Okamura Y, Iwamoto D, Noritsugu T, Mukai T. Development of pneumatic artificial rubber muscle using segmented shape-memory polymer sheets. J Robot Mechatronics 2023;35(1):113–24. http://dx.doi.org/10.20965/jrm.2023.p0113.
[26] Yahara S, Wakimoto S, Kanda T, Matsushita K. McKibben artificial muscle realizing variable contraction characteristics using helical shape-memory polymer fibers. Sensors Actuators A: Phys 2019;295:637–42. http://dx.doi.org/10.1016/j.sna.2019.06.012.
[27] Tondu B. Modelling of the McKibben artificial muscle: A review. J Intell Mater Syst Struct 2012;23(3):225–53. http://dx.doi.org/10.1177/1045389x11435435.
[28] Ashwin KP, Ghosal A. A survey on static modeling of miniaturized pneumatic artificial muscles with new model and experimental results. Appl Mech Rev 2018;70(4). http://dx.doi.org/10.1115/1.4041660.
[29] Guan Q, Sun J, Liu Y, Wereley NM, Leng J. Characterization and nonlinear models of bending extensile/contractile pneumatic artificial muscles. Smart Mater Struct 2021;30(2):025024. http://dx.doi.org/10.1088/1361-665x/abd4b0.
[30] Xu Q, Ying C, Zhang K, Xie H, E S. An effective nonlinear dynamic formulation to analyze grasping capability of soft pneumatic robotic gripper. Int J Smart Nano Mater 2024;15(3):405–31. http://dx.doi.org/10.1080/19475411.2024.2357313.
[31] Zhou Y, Cui H, Chen J. Geometric modeling of 3D woven composite tube RVE with cross-section variations. Fibers polym 2024;25(10):3945–56. http://dx.doi.org/10.1007/s12221-024-00691-5.
[32] Stella F, Guan Q, Della Santina C, Hughes J. Piecewise affine curvature model: a reduced-order model for soft robot-environment interaction beyond PCC. In: 2023 IEEE international conference on soft robotics. roboSoft, IEEE; 2023, p. 1–7. http://dx.doi.org/10.1109/robosoft55895.2023.10121939.
[33] Kim B, Lee SB, Lee J, Cho S, Park H, Yeom S, Park SH. A comparison among neo-hookean model, mooney-rivlin model, and ogden model for chloroprene rubber. Int J Precis Eng Manuf 2012;13(5):759–64. http://dx.doi.org/10.1007/s12541-012-0099-y.
[34] Wang G, Wereley NM, Pillsbury T. Non-linear quasi-static model of pneumatic artificial muscle actuators. J Intell Mater Syst Struct 2014;26(5):541–53. http://dx.doi.org/10.1177/1045389x14533430.
[35] Kalita B, Leonessa A, Dwivedy SK. A review on the development of pneumatic artificial muscle actuators: Force model and application. Actuators 2022;11(10):288. http://dx.doi.org/10.3390/act11100288.
[36] Visan AL, Alexandrescu N, Nita I. An application of finite element modeling to pneumatic artificial muscle from FESTO. Adv Mater Res 2012;463–464:818–21. http://dx.doi.org/10.4028/www.scientific.net/amr.463-464.818.
[37] Xiao W, Hu D, Chen W, Yang G, Han X. Design, characterization and optimization of multi-directional bending pneumatic artificial muscles. J Bionic Eng 2021;18(6):1358–68. http://dx.doi.org/10.1007/s42235-021-00077-w.
[38] Zabihollah S, Moezi SA, Sedaghati R. Design optimization of a miniaturized pneumatic artificial muscle and experimental validation. Actuators 2023;12(6):221. http://dx.doi.org/10.3390/act12060221.
[39] Tu Q, Wang Y, Yue D, Dwomoh FA. Analysis on the impact factors for the pulling force of the McKibben pneumatic artificial muscle by a FEM model. J Robot 2020;2020:1–11. http://dx.doi.org/10.1155/2020/4681796.
[40] Nozaki T, Noritsugu T. Motion analysis of McKibben type pneumatic rubber artificial muscle with finite element method. Int J Autom Technol 2014;8(2):147–58. http://dx.doi.org/10.20965/ijat.2014.p0147.
[41] Zhou Z, Ai Q, Meng W, Liu Q, Xie SQ, Zhou W. Design and finite element modeling of novel flat pneumatic artificial muscles. In: 2022 IEEE/aSME international conference on advanced intelligent mechatronics. AIM, IEEE; 2022, http://dx.doi.org/10.1109/aim52237.2022.9863322.
[42] Bashir MA. Use of dynamic mechanical analysis (DMA) for characterizing interfacial interactions in filled polymers. Solids 2021;2(1):108–20. http://dx.doi.org/10.3390/solids2010006.
[43] Zorlu A, Ozsoy C, Kuzucu A. In: Experimental modeling of a pneumatic system, vol. 1, 2004, p. 453–61. http://dx.doi.org/10.1109/etfa.2003.1247742.
[44] Wu X, Huang W, Zhao Y, Ding Z, Tang C, Zhang J. Mechanisms of the shape memory effect in polymeric materials. Polymers 2013;5(4):1169–202. http://dx.doi.org/10.3390/polym5041169.
[45] Tang Z, Guo L, Xu M, Ruan H, Yang J, Wang T, Zhang J, Wang Q, Zhang Y. Tribological behavior of shape memory cyanate ester materials and their tunable friction mechanism. Friction 2023;11(10):1794–803. http://dx.doi.org/10.1007/s40544-022-0689-3.
[46] Ghosh P, Srinivasa A. A two-network thermomechanical model and parametric study of the response of shape memory polymers. Mech Mater 2013;60:1–17. http://dx.doi.org/10.1016/j.mechmat.2012.12.005.
[47] Seo H-J, Kim YK, Hong SH, Lim SK. Energy harvesting and storage using highly durable biomass-based artificial muscle fibers via shape memory effect. Chem Eng J 2025;504:158850. http://dx.doi.org/10.1016/j.cej.2024.158850.
[48] Sun Y, Yang Z, Tao L, Wang Q, Zhang X, Zhang Y, Wang T. Rubber-assisted and modulated epoxy topological network for developing fatigue-resistant, high-strain-cycle high performance shape memory polymer composites. React Funct Polym 2024;106095. http://dx.doi.org/10.1016/j.reactfunctpolym.2024.106095.
[49] Cui Y, Lin J, Zhai Y, Xu C, Chen C, Chang C. Hydration programmable, shape memorable artificial muscles for antagonistic movements. Adv Funct Mater 2024;34(34). http://dx.doi.org/10.1002/adfm.202401005.